We are IntechOpen,
the world's leading publisher of Open Access books
Built by scientists, for scientists

6,100
Open access books available

149,000
International authors and editors

185M
Downloads

154
Countries delivered to

Our authors are among the

TOP 1%
most cited scientists

12.2%
Contributors from top 500 universities

WEB OF SCIENCE™

Selection of our books indexed in the Book Citation Index
in Web of Science™ Core Collection (BKCI)

Interested in publishing with us?
Contact book.department@intechopen.com

Numbers displayed above are based on latest data collected.
For more information visit www.intechopen.com

Chapter

Extended Lattice Light-Sheet with Incoherent Holography

Mariana Potcoava, Christopher Mann, Jonathan Art
and Simon Alford

Abstract

Recently, lattice light-sheet instruments and imaging technology have shown a great improvement in exploring the dynamics of life at subcellular resolution. However, to reconstruct 3-dimensional structures the objective lens or the sample stage are invariably moved. Invention of incoherent holography lattice light-sheet (IHLLS) using FINCH provides quantitative information on the state and size of subcellular changes of neurons over the visible spectrum. The technique allows both faster three-dimensional amplitude as well as phase imaging without moving either sample stage or the detection objective. Amplitude and phase measurements provide intrinsic instrumental simplicity, larger scanning area, and higher resolution when compared to the original LLS schemes. IHLLS is built as an additional detection arm of an original lattice light-sheet (LLS) system. In this chapter, we review the evolution of IHLLS to address its feasibility and limitations.

Keywords: fluorescence, incoherent holography, lattice light-sheet

1. Introduction

Neurons in situ are inherently 3-dimensional structures, with processes that extend through the nervous system in all dimensions. Volumetric imaging solutions that have been applied to this include confocal imaging, multiphoton imaging, and light sheet methods [1, 2]. With conventional approaches it is not possible to image in the millisecond temporal range at multiple depths. Light sheet approaches have rather poor z-axis resolution of 4 to 10 μm and suffer from substantial light sheet divergence within refractive tissue. Lattice light-sheet (*LLS*) imaging [3, 4] goes some way to resolving those issues. Sheet scanning allows individual frames to be captured at rates limited by the camera frame rate, and the lattice structure allows both high z-plane resolution (close to diffraction limited; approximately 400 nm) and good tissue penetration (up to 100 μm) in brain slices. However, despite the substantial contribution of the LLS groups to the biomedical imaging, and that z plane scanning of the lattice sheet can be rapid using galvanometers, the goal of imaging biological cells using LLS systems without moving the detection objective or the sample stage has not yet been achieved.

To overcome these hurdles, we built an incoherent holography lattice light-sheet (IHLLS) [5–7] tool as a second detection module of the original LLS system, with the

capability to image quantitative phase information of biological samples without moving the detection objective or the sample stage. The IHLLS system was first developed for the excitation wavelength 488 nm and emission wavelength 520 nm, but it can be further developed into a color imaging system, called incoherent color holographic lattice light-sheet (ICHLLS).

Phase imaging of live cells and tissue opens several possibilities that have not been available to more established methods in microscopy [8–23]. The simplest example is the ability of holographic imaging to reconstruct 3-dimensional information by both effectively autofocusing and extending the depth of field from which valuable information can be gathered. Taking the nervous system as an example, in dendritic fields, neurons receive information rapidly and often synchronously at different locations at various 3-dimensional planes. Neurons also respond electrically to inputs. This activity is rapid (milliseconds duration) and spreads throughout their complex 3D structure. Interestingly, changes in the entire cell membrane follow rapidly from localized electrical changes, and these can be detected in phase images in transmission or reflection imaging modalities [24]. This opens the possibility of measuring excitability of nerve cells across the complex 3-dimensional structure of the neuron. At longer time scales, organelle and protein movement within cells change the local refractive index [25]. Since phase changes in reflection geometry do not include the refractive index difference between the cytoplasm and the medium, it implies that the movements restricted to structural changes, axonal transport, or vesicle recycling may be detected through the cell membrane dynamics using the reflection phase microscopy approach.

Synaptic transmission, which requires precise coupling between action potentials, Ca^{2+} entry and neurotransmitter release [26], is also fundamental to the function of the brain. Thus, understanding synaptic function is key to understanding how the brain works while similarly, understanding synaptic dysfunction is crucial to understanding diseases of the brain. One key to understanding synaptic function is to image the distributed spatiotemporal axonal, dendritic, and synaptic activity in 3-dimensional space simultaneously and with high resolution. Our long-term aim will be to record phase changes evoked by synaptic activity within small (e.g. pre- and post-synaptic structures of the brain) in the millisecond time periods during which this activity occurs. The combination of LLS excitation targeting specific neurons with holographic phase imaging of selective fluorescent markers, called IHLLS, to detect fast events, or of electrical or structural changes of phase, creates many new approaches in imaging neuronal activity.

In this chapter, we will review the fundamental concepts, design, calibration, optimization, and terminology of IHLLS systems and discuss their imaging capabilities. We will begin with an overview of the IHLLS principle. We will then focus on each imaging system, IHLLS 1L and IHLLS 2L, with one or two excitation wavelengths, as well IHLLS in two colors, 488 and 560 nm, called ICHLLS. Applications suitable for phase modulation using incoherent light of neuronal cells will be discussed. At the end of the chapter, we will draw our conclusions and recommendations.

2. Incoherent holographic lattice light-sheet (IHLLS)

IHLLS [5–7] is a new imaging technique. It is a noninvasive, noncontact, and cross-sectional imaging method, that provides the imaging capability to build the 3D complex amplitude volume of neuronal cells with resolution comparable to, or better than

the resolution of the conventional LLS in dithering mode [3, 4] and with an extended FOV.

IHLLS operates as an extra detection module added on an existing LLS and utilizes the excitation technology of the LLS system, **Figure 1a**, in which excitation light is confined to a plane defined by a lattice of intersecting Bessel beams that self-reinforce as they project through tissue. Imaging detection uses the Fresnel incoherent correlation holography (FINCH) [27–31] principle. FINCH uses the self-interference property of the emitted fluorescent light to create Fresnel holograms of a 3D object in combination with the phase-shifting concept in which three or four interference patterns are created by a single channel on-axis interferometer. The beam splitter of the interferometer is replaced by a spatial light modulator (SLM), so that each spherical beam propagating from each 3D object's points is split into two spherical beams
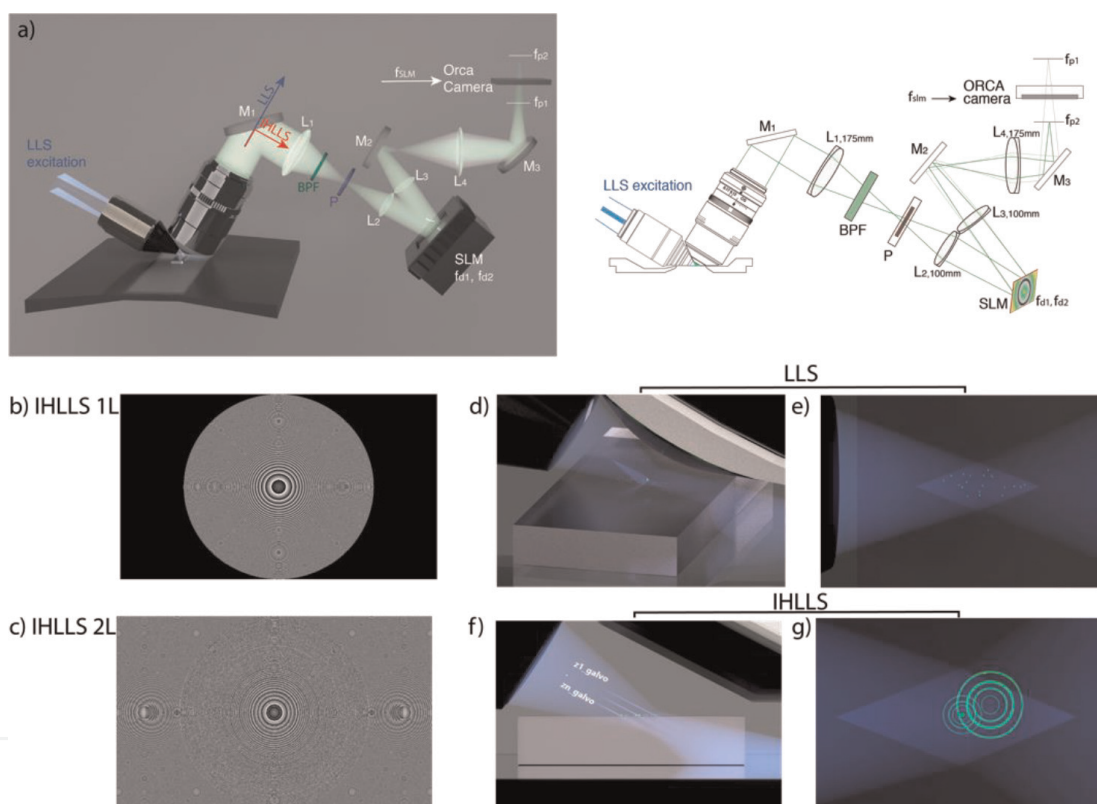
Figure 1.
The IHLLS system. (a) Schematics of the IHLLS systems with (b) one diffractive lens of focal length, $f_{SLM} = 400$ mm at the phase shift $\theta_1 = 0$, and (c) two diffractive lenses with focal lengths $f_{d1} = 220$ mm and $f_{d2} = 2356$ mm, at the phase shift $\theta_1 = 0$, superposed with a slight defocus to bring the objects in focus in the middle of the camera FOV; The system consists of a water immersed microscope objective MO (Nikon 25X, NA 1.1, WD 2 mm), lenses $L_1 = L_4$ with focal lengths 175 mm, $L_2 = L_3$ with focal lengths 100 mm; mirrors M_1, M_2, M_3; polarizer P; 520 nm center wavelength, 40 nm band pass filter BPF; spatial light modulator SLM. The light propagates through either pathway 1 (blue line in (a) for the original LLS or pathway 2 (red line in (a)) for IHLLS, depending on the orientation of sliding mirror. A collimated 30 Bessel beam is focused by an excitation objective lens (d, f) which generates a lattice light sheet. The vectors represent the x, y, z and s planes of the Bessel. z and x are moved by the z and x galvos. It excites only fluorophores in the focal plane (e) and in/off the focal plane (g) of the detection objective lens. While the z-galvo and z-piezo are moved along the z axis to acquire stacks in LLS (d-e), in IHLLS only the z-galvo is moved at various z positions (f-g), (Video_1 available at: https://bit.ly/3U4Iivy). For IHLLS, the size of the beam coming out the objective is diminished in half by the relay lens system, L_1 and L_2, to fit the size of the SLM. The SLM plane is optically conjugated with the objective back-focal-plane. The diffraction mask was positioned for all experiments on the anulus of 0.55 outer NA and 0.48 inner NA. The CMOS camera, tube lens, filter, and detection objective lens are used for fluorescence detection. The detection magnification M_{T-LLS}=62.5 and the illumination wavelength $\lambda_{illumination} = 488$ nm. The width of the light sheet in the center of the FOV is about 400 nm. x-axis is the direction of the x-galvo mirror motion, z-axis is the direction of the z-piezo mirror motion, and s-axis is the direction of excitation light propagation.

with different radii of curvature. The interference patterns from sample points are added incoherently, to further create Fresnel holograms. These holograms are numerically processed by in-house diffraction software.

So far, a short overview about the evolution of *IHLLS* devices was introduced. The following section will discuss various *IHLLS* systems and their technologies.

2.1 IHLLS systems and devices

We developed the IHLLS in two forms, with one diffractive lens and a constant phase with shared pixels, IHLLS 1L **Figure 1b**, **d**, **e**, or two diffractive lenses with randomly selected pixels, IHLLS 2 L (**Figure 1c**, **f**, **g**). The IHLLS 1L technique is used for calibration purposes and the IHLLS 2 L technique is used for the actual 3D sample imaging. The z-scanning principle in IHLLS 1L, same as in LLS, **Figure 1d**, **e**, is that both the z-galvanometric mirror (z-galvo) and the detection objective (z-piezo), synchronize in motion to scan the sample in 3D, but the axial resolution could be lower than the axial resolution in LLS due to the blurring effect of the constant phase lens added on the SLM that focusses to infinity. In IHLLS 2L, **Figure 1f**, **g**, the detection objective is kept fixed, but the z-galvanometric mirror moves to reach various depths in the sample and to increase the visibility of the Fresnel patterns.

2.1.1 IHLLS theoretical principle

The emitted light from a point object located in the front focal plane of the detection objective is collimated into a plane wave after passing the objective. This wave is transformed into two beams due to the two diffractive lenses with different focal lengths, f_{d1} and f_{d2}, uploaded on the SLM that focus at two focal points, f_{p1} and f_{p2}, **Figure 1a**. In the original setup of FINCH there are no optics between the microscope objective and the SLM or between the SLM and camera. Therefore, the focal lengths of the diffractive lenses coincide with their imaging distances, calculated from the SLM position toward the camera position. In this case the focal lengths of the diffractive lenses, f_{SLM}, f_{d1}, and f_{d2}, uploaded on the SLM, are different than their imaging planes measured from the SLM toward the camera. The beam is adjusted in size by using the two lens pairs, L_1, L_2 and L_3, L_4, to fit the SLM chip area. The SLM used here was a phase SLM (Meadowlark; 1920×1152 pixels, it was recalibrated to produce the desired focal lengths and phase shifts for a 520 nm wavelength and delivers a full 2π phase shift over its working range of 256 gray levels.

A hologram is obtained by the interference between the two positive spherical waves converging to the image points f_{p1}, and f_{p2} (relative to the SLM-plane), **Figure 1a**, located at -109 and 289 mm from the CMOS ORCA camera plane, and with interference efficiency $\tan(\varphi) \leq 0.04$.

Referring to eq. 16 from [29], $\tan(\varphi) \cong \frac{2R_0}{z_h} \leq \frac{\lambda}{2\delta_c}$, we get $0.03234 \leq 0.04$, where $R_0 = \max(R_{01}, R_{02}) = \max(11.393\ mm, 9.781\ mm) = 11.393\ mm$, R_{01}, R_{02} are the radii of the two beams at the exit of lens TL_4, $z_h = 664\ mm$, is the distance from TL_4 to camera, $\lambda = 520\ nm$ the emission wavelength, and $\delta_c = 6.5\ \mu m$ is the camera pixel size.

The SLM transparency containing the two diffractive lenses has the expression: $\left[C_1 Q\left(-\frac{1}{f_{d1}}\right) + C_2 \exp(i\theta) Q\left(-\frac{1}{f_{d2}}\right) \right]$, where $Q(b) = \exp\left[i\pi b\lambda^{-1}(x^2 + y^2)\right]$ is a quadratic phase function with (x, y) being the space coordinates, θ is the phase shift of the SLM, and C_1, C_2 are constants. When the system works in IHLLS 2L mode, $C_1 = 0.5$, $C_2 = 0.5$. When $f_{d1} = \infty$ (IHLLS 1L), the expression becomes:

$\left[C_1 + C_2 \exp (i\theta) Q \left(-\frac{1}{f_{SLM}} \right) \right]$, and $C_1 = 0.1$, $C_2 = 0.9$. Let us suppose the two waves, created by the diffractive lenses at the SLM, have the general expressions:

$$U_1(u, v) = A_1(u, v) \exp (i\phi_1(u, \ v)) \tag{1}$$

$$U_2(u, v) = A_2(u, v) \exp (i\phi_2(u, \ v) + \theta) \tag{2}$$

where (u, v) are the coordinates of the camera plane. With the assumption that the object is an infinitesimal object point, the intensity of the hologram at the sensor plane takes the following expression:

$$I_H(u, v) = |A_1(u, \ v)|^2 + |A_2(u, \ v)|^2 \tag{3}$$
$$+2 * A_1(u, v)A_1(u, v) \cos (\phi_1(u, \ v) - \phi_2(u, \ v) - \theta)$$

Then, four phase-shifted holograms with phase shifts applied to one of the diffractive lenses of 0, $\pi/2$, π, $3\pi/2$, are recorded by the camera and superposed using the phase-shifting algorithm to build the complex hologram of the object point at the camera plane:

$$U(u, v) = A(u, v) \exp (i\phi(u, \ v)) = $$
$$\frac{1}{4} \left\{ \left(I_{H(u, \ v, \ 0)} - I_{H(u, v, \ \pi)} \right) + i \left(I_{H\left(u, \ v, \ \pi/2 \right)} - I_{H\left(u, \ v, \ 3\pi/2 \right)} \right) \right\} \tag{4}$$

where: $A(u, v)$ is the amplitude of the encrypted image, which is the product of the two amplitudes, $A(u, v) = A_1(u, v) * A_2(u, v)$, and the encrypted phase:

$$\varnothing = \phi_1(u, v) - \phi_2(u, v) = arctan \left[\frac{I_H(u, \ v, \ \pi/2) - I_H(u, \ v, \ 3\pi/2)}{I_H(u, \ v, \ 0) - I_H(u, \ v, \ \pi)} \right] \tag{5}$$

Therefore, the complex amplitude distribution of the object wave at the camera plane has the expression:

$$A_1(u, v) \exp (i\phi(u, \ v)) = U(u, v)/A_2(u, v) \tag{6}$$

The 3D image of the object is retrieved by using the angular spectrum method to reconstruct the complex amplitude of the object wave at any depth within the positive reconstruction distance z_r, found by the expression:

$$z_r = \pm \frac{\left(z_h - f_{p1} \right) \left(f_{p2} - z_h \right)}{f_{p2} - f_{p1}} \tag{7}$$

We used the following values for the dual lens FINCH: $f_{p1} = 555.185$ mm, $f_{p2} = 826.793$ mm. The two focal lenses were calculated using OpticStudio (Zemax, LLC) in a multiconfiguration system as described in our previous work [5]. The distance between the last lens in the system, L4, and the camera was calculated by the optical design software as being $z_h = 664$ mm and matches the value calculated with the expression $z_h = \frac{2f_{p1}f_{p2}}{f_{p2} + f_{p1}}$. Therefore, using Eq. (7), the reconstruction distance is $z_r \cong 63$ mm, (in terms of lens distances) above and below the middle position of the z-galvo scanning range. If we need to reach out to the most extreme parts of objects in

the FOV of camera the reconstruction distance could increase to 8 mm. This distance corresponds to a *z-galvo* range of $z_{galvo} = \pm 40$ μm (in terms of object distances). This displacement is obtained for the LLS diffraction mask positioned on the anulus of outer NA of 0.55 and inner NA of 0.48, which generated a Bessel beam with a FWHM sheet length of 15 μm.

2.1.2 IHLLS optical design

We implemented the IHLLS approach in four main steps. *First*, we matched the effective pixel size in both configurations, conventional LLS and IHLLS 1L, **Figure 1f**, **g**, by using a USAF 1951 resolution target, **Figure 2a-d** and Opticstudio (Zemax, LLC) optical design, **Figure 2e-g**. The Opticstudio software simulated the optical components, beams propagation from the sample plane to the camera plane and calculated the correct distances between each sequential optical component. *Second*, we demonstrated the 3D imaging capabilities of polystyrene beads by using both conventional LLS and IHLLS 1L for the diffractive lens with f_{SLM} = 400 mm at phase $\theta = 0$ on the SLM, with x, z-galvo, and z-piezo motions, **Figure 3**, for the calibration purposes. *Third*, we have recorded and reconstructed IHLLS 2L bead holograms at various z-galvo scanning depths, from $-40 \ \mu m$ to $+40 \ \mu m$ in steps of $10 \ \mu m$, without moving the z-piezo, to assess the instrument performance in comparison to those of the conventional LLS, **Figure 4a-h**. *Fourth*, volumetric imaging of nerve cells **Figures 5–7** at 488 nm excitation wavelength, and color imaging, **Figure 8**, at dual excitation wavelengths, 488 and 560 nm, are presented.

It was determined that for an emission wavelength of 520 nm, and with an overall transversal magnification set to 62.5, the distances should be $d_1 = 75 \ mm$, $d_2 = 95.074 \ mm$, $d_3 = 288.914 \ mm$, $d_4 = 103.660 \ mm$, $d_5 = 103.660 \ mm$, $d_6 = 288.914 \ mm$, and the distance between the lens TL_4 to the detector should be 664 mm (i.e., $d_7 = 664 \ mm$), and the focal length of the single diffractive lens superimposed on the SLM was determined to be $f_{SLM} = 400 \ mm$. For this step, the transversal magnification of 62.5 was checked by imaging the USAF 1951 resolution target, group 7, element 6, with both instruments using a white light source. An optimization of a multi-configuration optical system, **Figure 2b**, **c**, were performed to
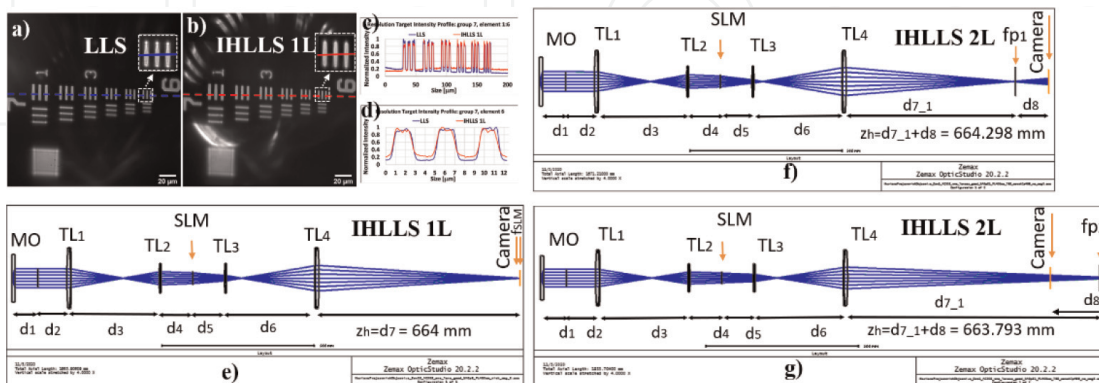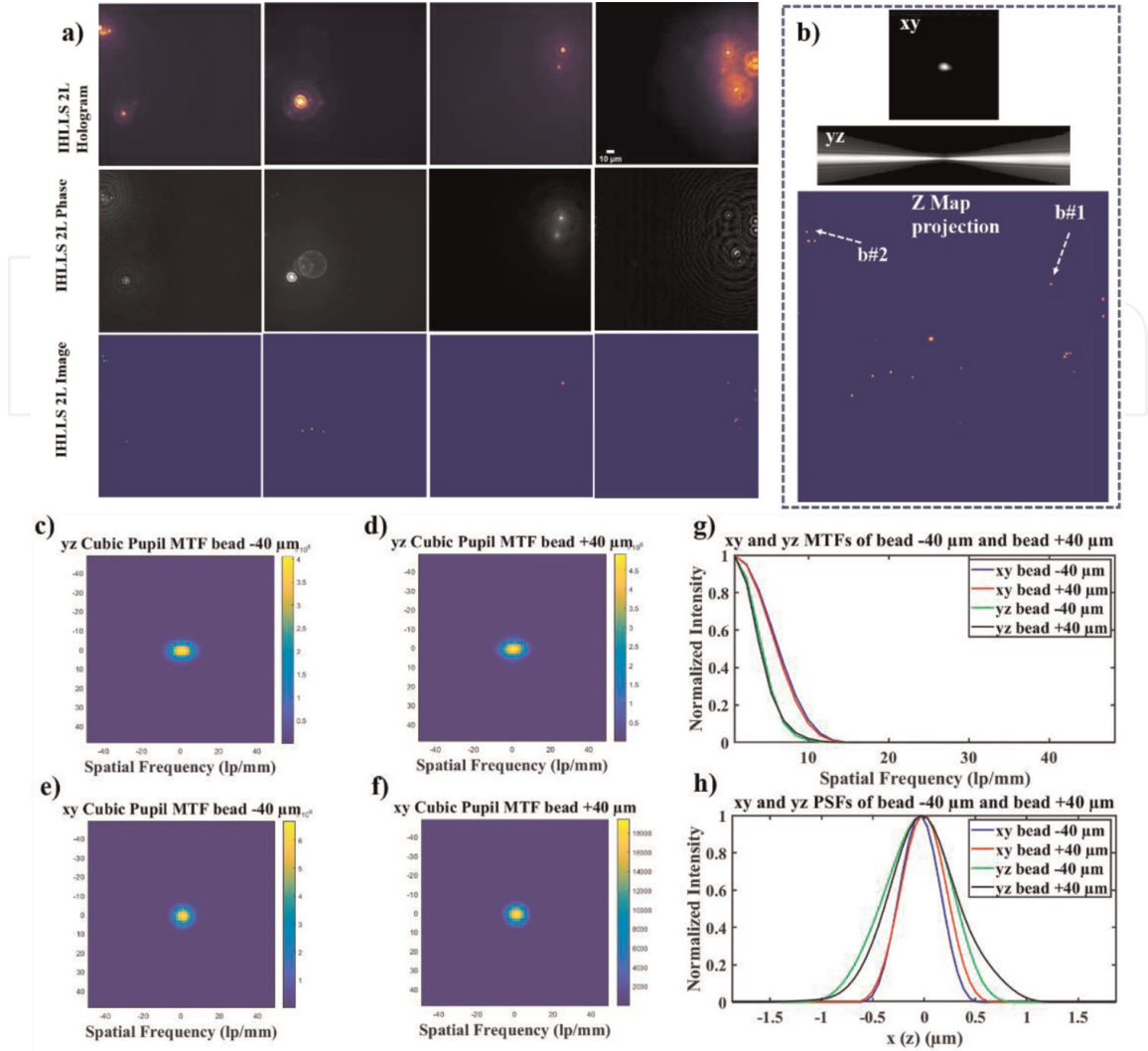

Figure 2.
Optical design of the IHLLS. (a) The LLS resolution target imaging (a, c (blue), d (blue)) with M_{T-LLS}=62.5; (b) The IHLLS resolution target imaging with one diffractive lens, IHLLS 1L, (b, c (red), d (red)) with $M_{T-IHLLS}$=62.5; (c), d, Cross-sections of group 7 and element 6 respectively; (e) Opticstudio simulation of IHLLS 1L, with the constraint $M_{T-IHLLS}$=62.5, to calculate the focal length (f_{SLM} = 400 mm) of a single diffractive lens uploaded on the SLM and the distances between each pair of optical components; (f), (g) These distances are kept constant for the simulation of IHLLS with two diffractive lenses, IHLLS 2L, to obtain the focal lengths of the two diffractive lenses on the SLM, f_{d1} = 220 mm and f_{d2} = 2356 mm.
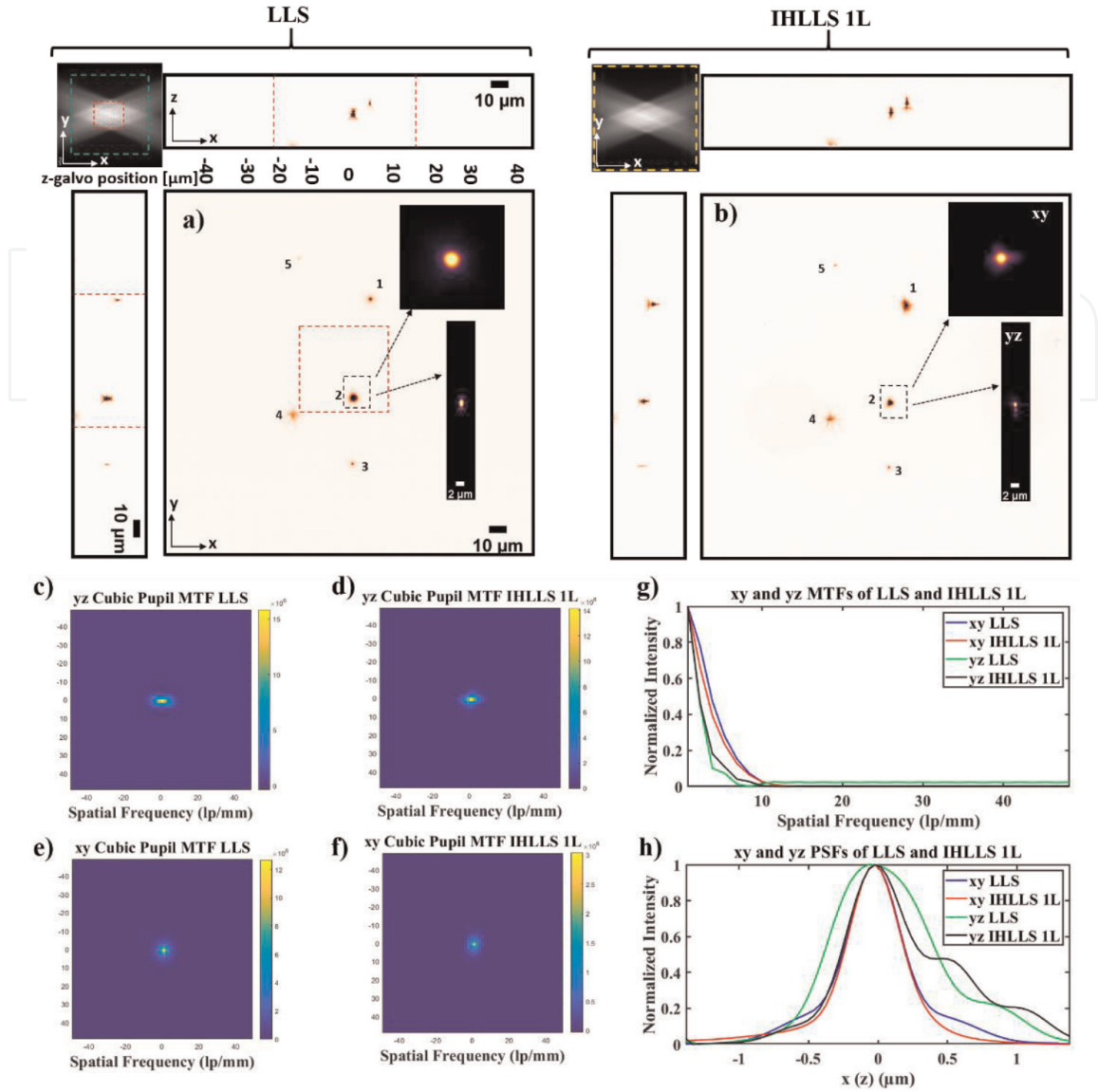
Figure 3.
Tomographic imaging of 0.5 μm, FOV 208 μm², in a conventional LLS (a) and incoherent LLS with only one diffractive lens (IHLLS 1L) of focal length 400 nm (b), without deconvolution. On the sides and above are shown the max projections through the volume (400 Z-galvo steps). The Bessel beams are displayed in the upper left corner of each xy-projection to show the orientation of the beams (FOV 208 μm²). The area enclosed inside the colored dashed rectangles are as follows: red- the scanning area for the original LLS (52 μm²), green – the extended area mentioned in [32] of 120 μm², and yellow – the actual scanning area for the LLS, IHLLS 1L, and IHLLS 2L. The bead #2 in the black dashed rectangle that is in the middle of the lattice sheet is considered for calculating the resolution for the two instruments. The transverse MTFs of the two imaging techniques are shown in (c, d) and the axial MTFs are shown in (e, f); (g) 1D xy and yz sections of the MTFs, (h) 1D xy and yz of the PSFs. The FWHM of the curves are blue- 0.530 μm, red 0.495 μm, green 0.8341 μm, and black 0.9004 μm.

calculate the focal lengths of the two diffractive lenses superimposed on the SLM to provide maximum overlap of the two beams at the plane of the detector but keeping fixed all the distances $d_1 \div d_7$ found in the previous step. After performing the optimization, the values of the two focal lengths were found to be $f_{d1} = 220\ mm$ and $f_{d2} = 2356\ mm$, which were used for the design of the two diffractive lenses. These two lenses focus at a distance of $d_{7\_1} = 555.185\ mm$ in the front of the camera, **Figure 2b**, and at $d_{7\_1} = 826.793\ mm$ behind the camera, **Figure 2c**, respectively. In implementation, the distance $d_{7\_1} + d_8$ may need to be tuned by ± 0.3 depending on tolerances and imperfections of optical parameters of other elements of the system
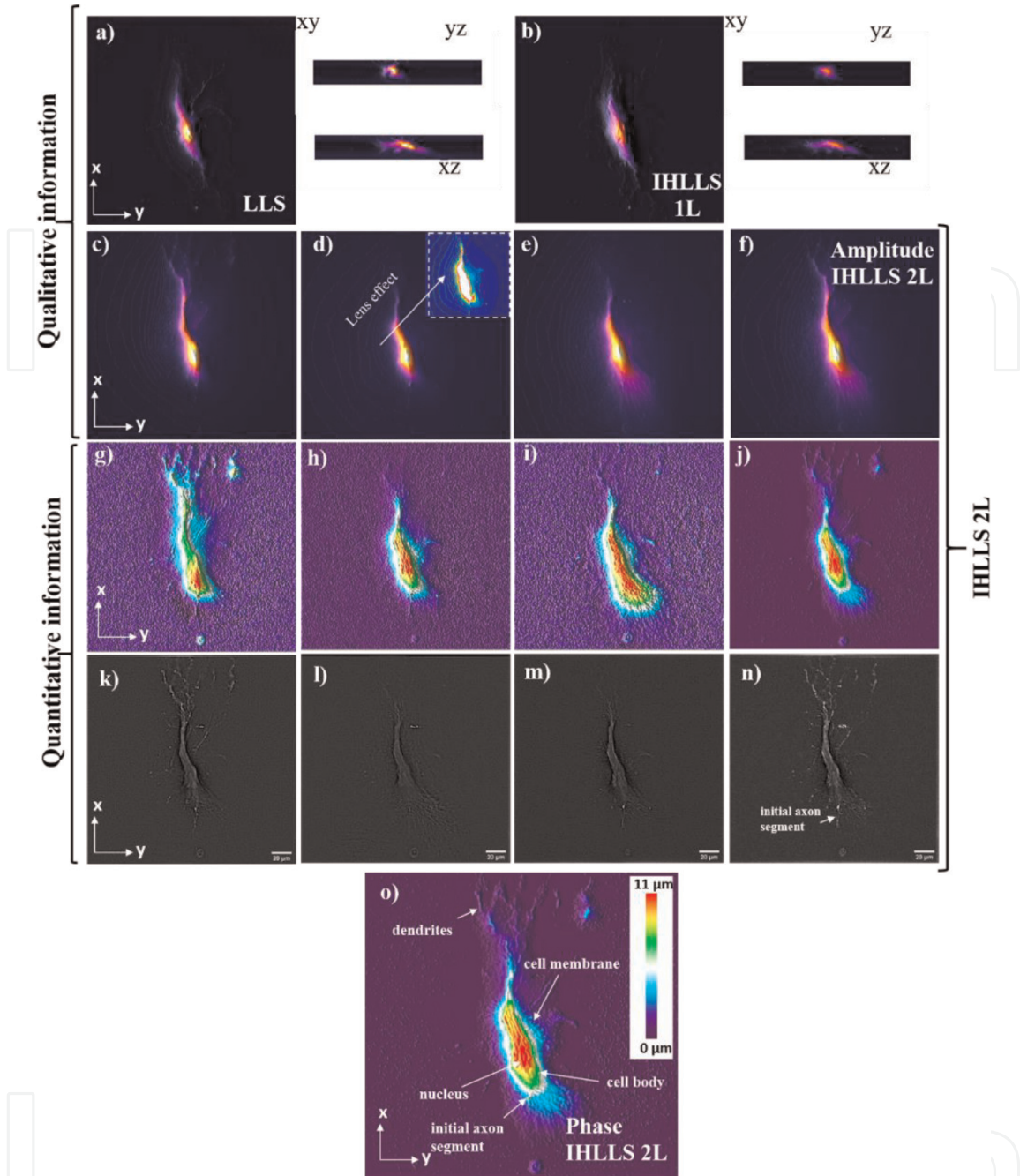
Figure 4.
IHLLS 2L beads volume reconstruction; (a) 500 nm beads holography ±40 μm, ± 30 μm, holograms (first row), phase maps (second row), and reconstructed images (third row); (b) The xy and yz cross-sections of a bead after the hologram reconstruction together with the z-max projection of all the best z-reconstructed planes. The IHLLS phase images contain the depth dependent phase information derived from the IHLLS holograms and the reconstructed IHLLS images show the complex holograms propagated to the best focal plane. The max projection of the reconstructed volume of the 500 nm beads sample contains the z-galvo levels ±40 μm, ± 30 μm, ± 20 μm, and 0 μm. The transverse MTFs of the two beads b#1 and b#2 are shown in (c, d) and the axial MTFs are shown in (e, f); (g) 1D xy and yz sections of the MTFs, (h) 1D xy and yz of the PSFs. The FWHM of the curves are blue-0.4534 μm, red 0.5118 μm, green 0.7663 μm, and black 0.7946 μm.

(e.g., tolerances of lenses, tolerances of phase resolution of the SLM, etc.). (i.e., $d_{7\_1} + d_8 = 664.298\ mm$, when calculating f_{d1}, and $d_{7\_1} + d_8 = 663.793\ mm$, when calculating f_{d2}.

2.1.3 IHLLS 1L calibration imaging

The first experiment was performed using the conventional LLS pathway where the z-galvo was stepped in $\delta z_{LLS} = 0.101\ \mu m$ increments through the focal plane of a 25x Nikon objective, which was simultaneously moved the same distance with a z-piezo controller for a displacement range of $\Delta z_{galvo} = 80\ \mu m$, **Figure 3a**, for scanning area of $208 \times 208\ \mu m^2$. The second set of images was obtained using the IHLLS 1L with focal length $f_{SLM} = 400\ mm$ displayed on the SLM, where both the z-galvo and
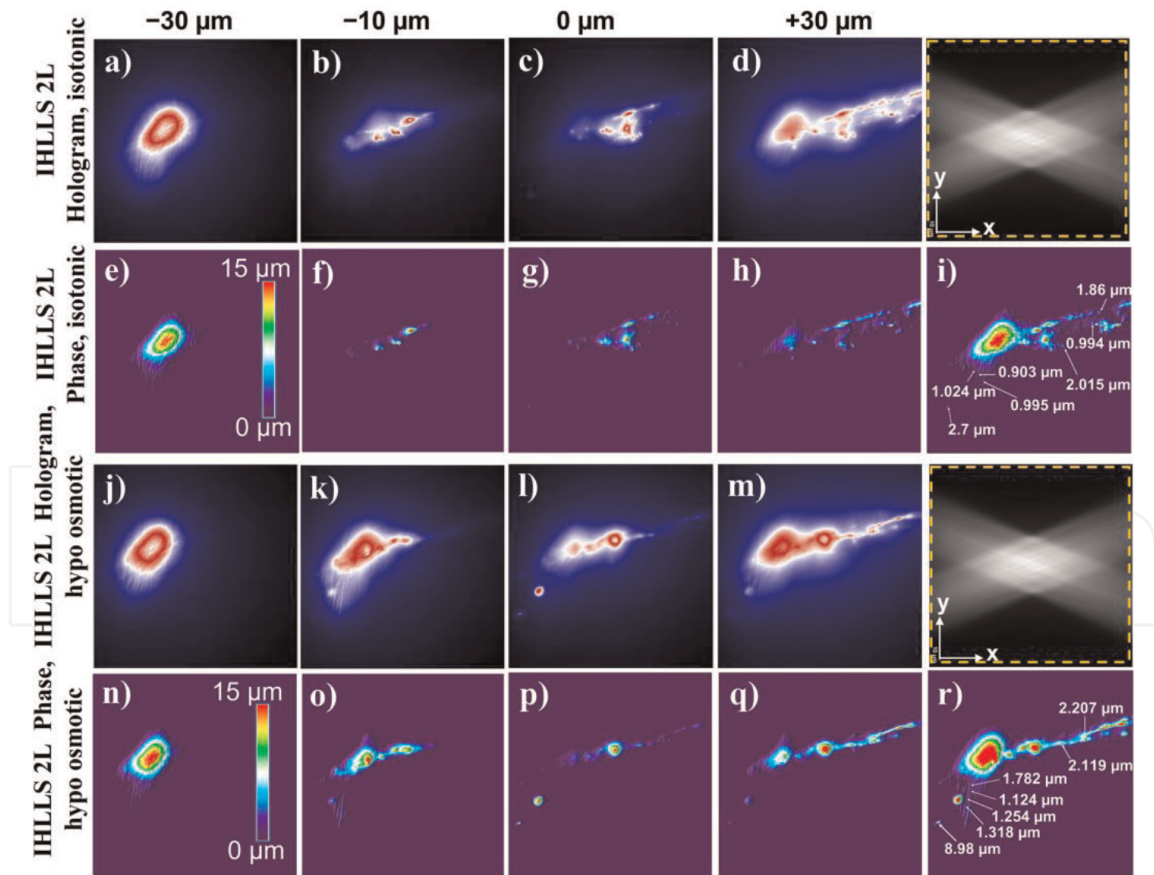
Figure 5.
Lattice light-sheet imaging of a lamprey spinal cord ventral horn neuron with dendrites; (a) Max projections through the volume (300 z-galvo steps) in a conventional LLSM without deconvolution; (b) Max projections through the volume (300 z-galvo steps) in an incoherent LLSM without deconvolution using IHLLS 1L; Amplitude reconstruction of a neuronal cell at three z-galvo positions: (c) + 30 μm, (d) 0 μm, (e) -30 μm, and (f) the superposition of all three; Phase reconstruction of a neuronal cell at z-galvo positions: (g) + 30 μm, (h) 0 μm, (i) -30 μm, and (j), (o) the superposition of all three; (k)-(n) Band-pass filter applied to the phase images from (g)-(j).

z-piezo were again stepped with the same $\delta z_{LLS} = 0.101\ \mu m$ increments through the focal plane of the objective for the same displacement $\Delta z_{galvo} = 80\ \mu m$, **Figure 3b**. The scanning area in a conventional LLS is at best $54 \times 54\ \mu m^2$ (red square in **Figure 3a** and in the upper left corner of **Figure 3a**), and it is too large for being illuminated by the Bessel beams. Therefore, to enlarge the scanned region these $54 \times 54\ \mu m^2$ areas can be moved in a mosaic-fashion by moving the sample. However, this requires a substantially longer acquisition time and image registration. It also prevents
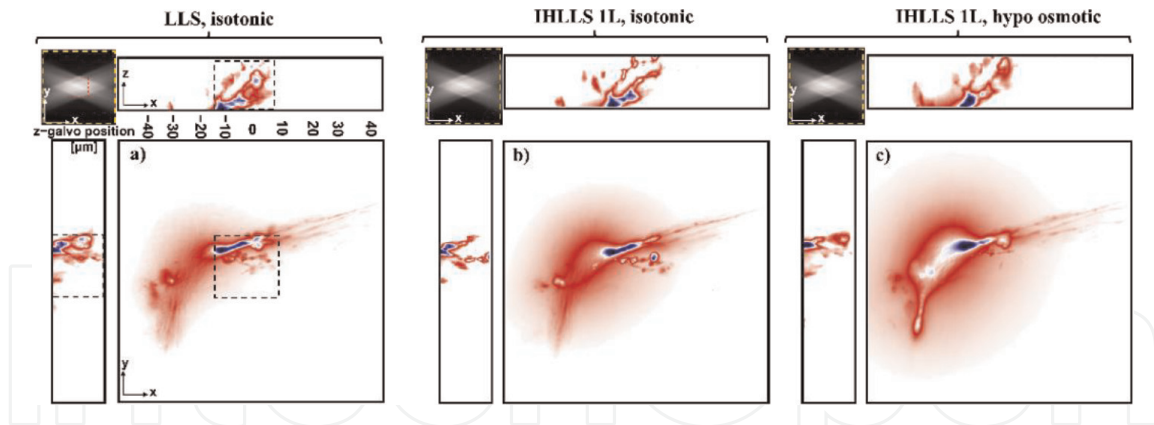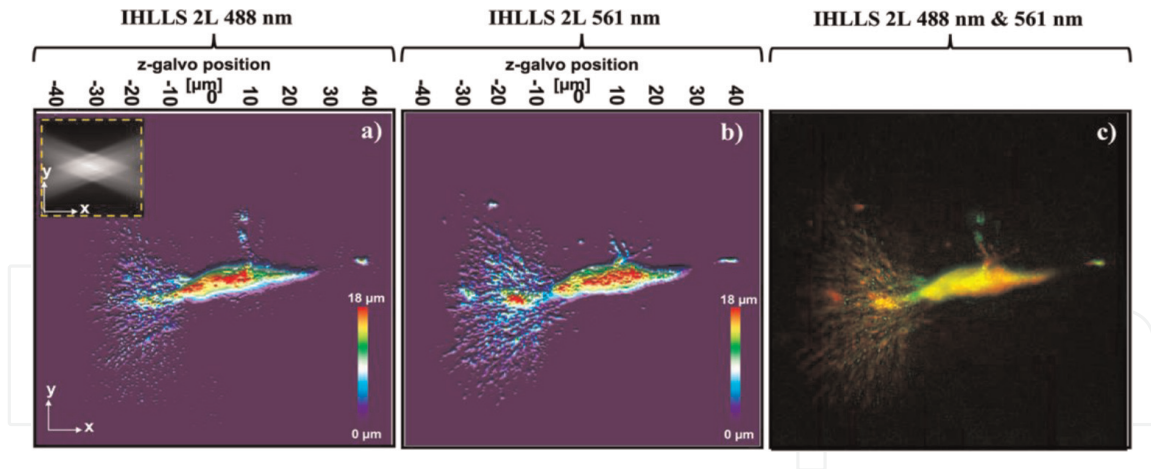
Figure 6.
Tomographic imaging of a lamprey spinal cord ventral horn neuron with dendrites, xy FOV 208 × 208 μm²,
*2048 × 2048 pixels, yz, (xz) FOV 208 × 40 μm², 2048 × 400 pixels, in a conventional LLS (a) and incoherent
LLS with only one diffractive lens (IHLLS 1L) of focal length 400 mm without deconvolution; recordings were
initially in isotonic solution (b), and then in hypotonic solution to cause swelling (c). On the sides and above are
shown the max projections through the volume (400 z-galvo steps). The Bessel beams are displayed in the upper-
left corner of each xy-projection to show the orientation of the beams (FOV 208 μm²). The area enclosed inside the
colored dashed rectangles are as follows: black—the scanning area for the original LLS (52 μm²), and yellow—the
actual scanning area for the LLS, IHLLS 1L, and IHLLS 2L.*

Figure 7.
*IHLLS 2L imaging of a lamprey spinal cord ventral horn neuron with dendrites in a Ringer's solution (a–i) and
hypotonic solution (j–r), FOV 208 × 208 μm², 2048 × 2048 pixels; (a–d, j–m) imaging holography at
−30 μm, − 10 μm, 0 μm, and +30 μm, for the phase-shift θ = 0; (e–h, n–q) the corresponding reconstructed
phase images; (i, r) the superposition of all reconstructed phase images at ±40 μm, ± 30 μm, ± 20 μm, ±
10 μm, and 0 μm. The Bessel beams are displayed in the right gray panel of each xy-projection to show the
orientation of the beams (FOV 208 × 208 μm²). The phase values of the reconstructed images were converted to the
optical path length values in reflection mode.*

Figure 8.
IHLLS-2L max projection of the reconstructed phase at 9 z_{galvo} positions, z_{galvo} = ±40 μm, ±30 μm, ±20 μm, ±10 μm, and 0 μm, at (a) 488 nm, (b) 561 nm, and (c) combination of (a) and (b). The scanning area in both experiments was 208×208 μm². The scanning area in IHLLS-2L is at best 208×208 μm².

simultaneous use of other recording modalities such as electrophysiology. A recent more effective solution is to extend the scanning area to $170 \times 170 \ \mu m^2$ (green square in the upper left corner of **Figure 3a**). This was achieved by superposing a spherical phase profile on the illumination wavefront at the pupil plane which requires 17 tiling positions [33], but with a lower axial resolution than the original LLS. The IHLLS 1L, **Figure 3b,d**, performs better than LLS by scanning a bigger area, but the resolution is lower in the axial directions due to the blurring effect of one of the lenses that is focused to infinity. Resolving fine structure in an image depends on both the shape and the extent of the spatial frequency support of the optical transfer function (OTF). To evaluate the relative imaging performance of IHLLS 1L compared with conventional LLSM techniques, the OTFs of these methods were computed in the following way. We calculated the xy- and yz- point spread functions of the two systems and compared them to the bead # 2's transverse and axial images. The absolute values of the OTFs were calculated for the xy and yx cross-sections, **Figure 3c-f**, by taking the Fourier transform of the 2D PSFs distributions. The 1D OTFs are shown in **Figure 3g** and the corresponding PSFs in **Figure 3h**.

We calculated the FWHM in xy and yz directions for the two systems by fitting the PSFs from **Figure 3h** with a 1D Gaussian function. The calculations for the 500 nm beads show a xy FWHM of 530 nm (LLS), 495 nm (IHLLS 1L) and yz FWHM of 834 nm (LLS) and 900 nm (IHLLS 1L). The IHLLS performs better within the scanning areas of $54 \times 54 \ \mu m^2$ and it gets worse outside this area due to the blurring effect of the second lens with infinite focal length.

2.1.4 IHLLS 2L calibration imaging

A step-by-step initiative in the *IHLLS system* has been the implementation of dual diffractive lenses comprising randomly selected pixels (*IHLLS 2L*) for recording sample holograms, **Figure 1c**. Only the z-galvo was moved within the same $\Delta z_{galvo} = 40 \ \mu m$ displacement range, above and below the reference focus position of the objective (which corresponds to the middle of the camera FOV), at $z_{galvo} = \pm 40 \ \mu m \pm 30 \ \mu m$, $\pm 20 \ \mu m, \pm 10 \ \mu m$, and $0 \ \mu m$. This approach enables full complex-amplitude modulation of the emitted light for extended FOV and depth.

The results are summarized in **Figure 4(a), (b)**, which depict the sample at four z-galvo planes, denoted $z_{galvo} = \pm 40 \; \mu m$, and $\pm 30 \; \mu m$. The z-galvo planes correspond to the same relative depths in the sample. The reconstruction distance calibration from the image plane to the sample plane is 20 mm in the IHLLS pathway for each $\pm 10 \; \mu m$ displacement of the z-galvo mirror so, it means the conversion should be 80 mm to $\pm 40 \; \mu m$.

The IHLLS 2L holograms ($\theta = 0$) for each z-galvo level are displayed in the upper row of **Figure 4a**), and the phase corresponding to each hologram displayed in the second row. The phase images contain the depth dependent phase information derived from the IHLLS holograms. Then, the complex hologram is propagated and reconstructed at the best focal plane using a custom diffraction Angular Spectrum method (ASM) routine programmed in MATLAB (MathWorks, Inc.). These IHLLS 2L reconstructed images are shown in the third row of **Figure 4a**. We chose the ASM and not the Fresnel reconstruction as the ASM can reconstruct the wave field at any distance from the hologram plane, without the minimum reconstruction distance requirement [9]. The max projection of all z-planes where the beads were found are displayed in **Figure 4b**. They show the complex holograms propagated to the best focal plane. We performed scanning at other three z-galvo levels, $\pm 10 \; \mu m$, and 0 μm, but the results are not shown in **Figure 4**. Each column of **Figure 4a** results from images captured with the z-galvo positioned at a designated sample plane. Consequently, a sample plane at $z_{galvo} = +40 \; \mu m$, contains the right layer of beads in this image, the sample plane at $z_{galvo} = -40 \; \mu m$ contains the left layer and sample planes at $\pm 30 \; \mu m \pm 20 \; \mu m$, and 0 μm, are equidistant between the two layers. We also determined the distribution in transverse FWHM values for the 500 nm beads, **Figure 4**.

2.2 Applications of IHLLS

In this part of the chapter, we will provide information on potential use of *IHLLS systems in neuroscience*. LLS volumetric imaging, **Figure 5a**, can provide only morphological measurements in any sample volume, but not complex cellular parameters such as the cellular dry mass or refractive index (RI) [16]. These are features of cells that dynamically change in response to activity. As an example, the LLS is unable to account directly for potential contributions that might be provided to the surface area by subresolution features such as subdiffraction sized structure including microvilli [32], whose structure can be rapidly altered by Ca^{2+} entry [34–36] or the structure of cell membranes altered by voltage fluctuations [37]. Therefore, quantitative analysis of cells and membrane dynamics detected by using the IHLLS system will be of significance in understanding a range of cell functions.

2.2.1 Imaging neurons

For this step we chose a simple neuronal preparation in which a neuron could be readily labeled with fluorescent dye and maintained alive during imaging. Lamprey spinal cord ventral horn neurons have dendrites that are sufficiently large to cover the whole camera FOV of 208 μm^2. When performing tomographic imaging using the original LLS, **Figure 5a**, or IHLLS 1L (phase $\theta = 0$ in **Figure 5b**), the sample outside of the maximum area of $78 \times 78 \; \mu m^2$ cannot be resolved, although the z-galvo mirror and the z-piezo stage objective were moved 300 steps in the range 60 μm. Deconvolution

sharpening of the raw data is the standard solution for blur reduction and enhancement of fine image details in LLS image processing. When using the IHLLS 2L, **Figure 5c**-**f**, the max projection of only three reconstructed amplitude images from IHLLS holograms recorded at $z_{galvo} = \pm 30 \, \mu m$, and $0 \, \mu m$, could give similar results as the LLS, and within a larger resolved sample area. In addition to the amplitude images, the IHLLS 2L can provide access to the reconstructed phase information, **Figure 5g**-**j**, needed to understand the physiology and pathophysiology of various cells or other parts of samples under study. Applying further a band-pass filter to the above phase images other features could be identified, **Figure 5k**-**n**.

Within biological samples, axial resolution enhancement is possible if the phase difference of two interfering wavefronts is known. The combination of the two lenses with focal lengths, f_{d1} = 220 mm and f_{d2} = 2356 mm, gave a reconstruction distance with a maximum 80 *mm* above the reference plane (microscope objective position or the middle of the camera FOV) and 60 mm below the reference plane, but when converted to the z-galvo displacement the reconstructed distance was 30 *μm* and $-30 \, \mu m$ respectively, which results in a 60 *μm* volume height. When the scanning range is increased to $\pm 40 \, \mu m$, the reconstruction distance increases to about 250 *mm* above the reference plane and 80 mm below the reference plane, which correspond to z-galvo displacements of 40 *μm* and $-40 \, \mu m$ respectively, and a 80 *μm* volume height.

3D perspective representation of the quantitative phase contrast image of the neuron is displayed in **Figure 5g**-**j**. Each pixel represents a quantitative measurement of the cellular optical path length (OPL) of the fluorescently labeled neurons and their subcellular compartments. The scale (at right) in **Figure 5o**) relates the OPL (in the color look-at table) to the morphology (in μm). The IHLLS 2L and LLS techniques have similar transverse performances, but the axial performance is poorer for the IHLLS 2L, when moving the z-galvo in 7 or 9 steps along the 80 μm ranges. Therefore, we need to increase the number of z-galvo increments to achieve a better axial performance.

2.2.2 LLS and IHLLS neuronal imaging at excitation wavelength 488 nm

Lamprey neurons were imaged in isolated spinal cords of newly transformed lampreys (*Petromyzon marinus*). Lamprey ventral horn neurons were fluorescently labeled with Alexa 488 hydrazide using previously published methods [6]. To ensure successful labeling of the neurons, the resultant epifluorescence was imaged during excitation with 470 nm LED illumination, and images were captured on an sCMOS camera (PCO AG, Kelheim, Germany). The chamber and spinal cord were then transferred onto the customized stage of the LLS microscope. The recording chamber was again continually superfused with cold, oxygenated Ringer (8–10°C) for the duration of the experiment. The labeled neurons were then imaged in this chamber using LLS and the osmotic potential of the superfusate changed by switching its input.

To examine the effects of applying IHLLS holography, we performed three experiments for this study for calibration purposes. The first was carried out using the conventional LLS pathway, where the *z-galvo* was stepped in $\delta z_{LLS} = 0.101$ μm increments through the focal plane of a 25x Nikon objective, which was simultaneously moved the same distance with a z-piezo controller for a displacement range of $\Delta z_{galvo} = 40$ μm, **Figure 6a**, for scanning area of $208 \times 208 \, \mu m^2$. The second set of images was obtained using the IHLLS 1L with focal length $f_{SLM} = 400$ mm, displayed on the SLM, where both the z-galvo and z-piezo were again stepped with the same

$\delta z_{\mathrm{LLS}} = 0.101$ μm increments through the focal plane of the objective for the same displacement $\Delta z_{\mathrm{galvo}} = 40$ μm. The intensity images using the IHLLS 1L mode were recorded only for the diffractive lens with phase shift $\theta = 0$.Initially, these images, obtained in both LLS and IHLLS 1L modes, were obtained in isotonic lamprey Ringer's solution (270mOsm, **Figure 6a**, **b**).

To expand the neurons as an initial test of the ability of the IHLLS system to record small changes in size, we repeated the experiment using the IHLLS 1L, where the Ringer's solution was modified with hypotonic solution (225mOsm), **Figure 6c**. The third step was achieved by combining the coherent properties of the Bessel beams with the incoherent properties of the fluorescent light emitted by each 3D point of the sample but made coherent in the self-interference process. This method was performed with both solutions, isotonic and hypotonic solutions, using the IHLLS pathway with two super-imposed diffractive lenses displayed on the SLM comprising randomly selected pixels (IHLLS 2L), where only the z-galvo was moved within the same $\Delta z_{\mathrm{galvo}} = 40$ μm displacement range, above and below the reference focus posi-tion of the objective (which corresponds to the middle of the camera FOV), at $z_{\mathrm{galvo}} = \pm 40$ μm ± 30 μm, ± 20 μm,± 10 μm, and 0 μm. The two wavefronts interfere with each other at the camera plane to create Fresnel holograms. Four interference patterns were created using a phase shifting technique ($\theta = 0$,$\theta = \pi/2$, $\theta = \pi$,$\theta = 3\pi/2$) and further combined mathematically to obtain the complex ampli-tude of the object point at the camera plane. The results are summarized in **Figure 7** which depicts the samples in isotonic, **Figure 7a–i**, or hypotonic solutions, **Figure 7j–r**, at four z-galvo planes, denoted $z_{\mathrm{galvo}} = \pm 30$ μm, -10 μm, and 0 μm. The z-galvo planes correspond to the same relative depths in the sample. Four holographic images were recorded for each z-galvo position and combined mathematically to build the complex amplitude of each sample. The 3D field was reconstructed at various depth positions, and those images in focus at certain planes were chosen to build the tomo-graphic structure of the neuron. We performed scanning at nine z-galvo positions and, therefore, nine phase images were selected to build the tomographic slice of all nine superposed images, **Figure 7i**, **r**. It is clear from this that the soma (**Figure 7e** compared to **Figure 7n**) and the dendrites (**Figure 7f–h** compared to **Figure 7o–q**) all showed an increase in volume. We have emphasized this by measuring the phase values of various points in the neuron's dendritic tree and calculating the optical path length that this represents, first in isotonic solution and then in hypo-osmotic solution. This treatment is expected to swell the neurons, including the dendritic tree, increasing the size of these structures. The analyses indicate that the technique can resolve sub-micrometer size changes, represented in depth by the color coding shown in **Figure 7**. For comparison, we measured the diameters of well separated structures in the xy plane, which are expected to be similar to the depth in these cylindrical structures. We have inserted these numbers in **Figure 7i**, **r**. The diameters measured increased from 1.41 ± 0.50 to 2.28 ± 1.04 μm. These are also clearly resolvable from the depth encoding.

2.2.3 LLS and IHLLS neuronal imaging at excitation wavelength 488 and 560 nm

Synchronous synaptic transmission, which requires precise coupling between action potentials, Ca^{2+} entry and neurotransmitter release [32], is fundamental to the function of the brain. Thus, understanding synaptic function is key to understanding how the brain works while similarly, understanding synaptic dysfunction is crucial to understanding diseases of the brain. One key to understanding synaptic function is to

image the spatiotemporal axonal, dendritic, and synaptic activity in 3-dimensional space simultaneously and with high resolution. Our long-term aim will be to record phase changes evoked by synaptic activity within small (e.g. pre- and post-synaptic structures of the brain) in the millisecond time periods during which this activity occurs. Here, we describe a general approach to 2 color phase imaging in neurons which give high spatial and temporal resolution.

We have expanded our newly developed single wavelength IHLLS microscope, with one (IHLLS – 1L) or two diffractive lenses (IHLLS-2L) [1], to a two wavelengths optical design and imaging technique. These two excitation beams, 488 and 561 nm, will produce corresponding emission beams at 523 and 570 nm respectively.

The two-color technique still uses the self-interference properties of the emitted fluorescent light [24], in which three or four interference patterns are created using a phase shifting technique, to create Fresnel holograms of a 3D object. However, the spatial light modulation (SLM) optical design configuration has been modified to actively control the dual diffractive lenses phase-shifting at two colors sequentially. This is repeated at each z-galvo scanning level. The technique allows both faster three-dimensional amplitude and phase imaging without moving either the sample stage or the detection objective, for extended FOV (208×208 mm^2) and depth. The scanning depth is a function of two variables, the numerical aperture of the LLS diffraction mask annulus and the z-galvanometer mirror scanning range. Using an anulus of 0.55 outer NA and 0.48 inner NA, the scanning depth could reach up to 80 μm, using 9 z-galvo positions within the range Δz_{galvo} = 80 μm, at z_{galvo} = ±40, ±30, ±20, ±10, and 0 μm.

The optical setup of the IHLLS system at one wavelength is covered in [1]. The two-color system is driven by the same principle. The system calibration is done simultaneously with one diffractive lens, IHLLS-1L, of focal lengths, $f_{SLM-488}$ = 400 mm, and $f_{SLM-561}$ = 415 mm respectively. After that, we perform sample scanning using two diffractive lenses with randomnly selected pixels, for each wavelength, with focal lengths f_{d1-488} = 220 mm, f_{d2-488} = 2356 mm, and f_{d1-561} = 228 mm and f_{d2-561} = 2444 mm. The physical distances between each sequential optical component and the the focal distances for the two excitation wavelengths, 488 and 561 nm, were calculated using Opticstudio (Zemax, LLC). We designed a multi-configuration optical system with the condition that the height of the two beams generated by the two lenses was equal in size at the camera plane for a perfect overlap.

To examine the effects of applying ICHLLS holography, neurons fluorescently labeled live *in situ* in the central nervous system (lamprey spinal ventral horn neurons), **Figure 8**, were used as test samples. Fluorescent dyes, Alexa Fluor™ 488 and 568 nm hydrazide, were injected by microinjection into the neuron.

3. Conclusions

The use of IHLLS enhances lattice light sheet microscopy in several ways.

- The optical and mechanical designs of the incoherent arm expand the applicability of the lattice light-sheet system and could open entirely new imaging modalities in all light sheet imaging instruments. The use of IHLLS enhances lattice light sheet microscopy in several ways. In the original FINCH system, it was shown that using spatial incoherent light, such as fluorescent light,

to form holograms, and producing images with better spatial resolution than conventional imaging, is possible, because the incoherent imaging systems break the Lagrange principle valid for classical imaging system. This occurs in such a way that it magnifies the gap between two spots more than it magnifies the spots themselves [38–40]. While we have indeed achieved higher resolution with IHLLS-2L than with IHLLS-1L or LLS, we must still do more work to optimize the system. We need to determine how many optimal galvanometric and hologram reconstruction steps are needed before we draw the same conclusion here. Another factor to consider is to investigate the Lagrange principle with a larger area SLM without the need to reduce and expand the beam size.

- In LLS focus of the emission objective must be maintained in the focal plane of the lattice sheet, requiring movement of a bulky objective, which takes time, but also at the high speeds of LLS imaging will apply fluid pressure movements across the sample. This will potentially distort images, but in addition will provide noise to transient measurements of cell surfaces caused by rapid activity, for example action potential firing in excitable cells. It is also difficult to resolve very small changes in surface structure at speed, even with volumetric imaging. Consequently, the ability to resolve rapid surface structure changes, without moving the objective lens and higher accuracies than traditional volumetric imaging approaches is valuable.

- We demonstrated the capacity of the IHLLS system to reconstruct 3D positions of beads as light point sources using a very reduced number of z-galvo mirror scanning planes when compared to the original LLS system using the dithered mode. We also showed the same or slightly improved resolution of the bead positions. The IHLLS system can therefore provide faster volumetric image acquisition and multi-plane imaging for probing the three-dimensional morphology and structure of biological samples. In this study we have demonstrated that IHLLS can be used to resolve artificially applied changes in neuron shape. We will seek in further studies to relate these changes to physiological activity.

- Although we eliminated the z-piezo objective motion needed to maintain the object focus, there are a few challenges in approaching this work. The conventional LLS system uses a very low dose of light and low exposure time without a polarizer in the detection path. The digital incoherent holography technique with two diffractive lenses uses two polarizers in the detection arm; therefore, the light dose and the exposure time must be increased from the middle of the z-galvo scanning range toward the two ends of the scanning range to maintain a similar signal efficiency as in the conventional LLS, but low enough to preserve the biological samples. For this reason, we opted out of using a double diffractive lens FINCH technique with randomly selected pixels which requires only one polarizer mounted before the SLM, to align the input beam to its active axis. The SLM was also positioned at 11° deflection angle to generate active beam steering at the highest efficiency. Another challenge in this configuration is the beam size of 17.6 mm in the back focal plane of the microscope objective (Nikon Apo LWD 25×1.1 W), which is too large for the SLM chip size (17.66×10.6 mm, Meadowlark Optics)), and we decided to place the SLM in a double 4f optic system configuration made by two lenses of 200 mm focal lengths and two lenses of 125 mm focal lengths. This combination has also helped to decrease the $z_{h\,min}$ to about 664 mm.

Conflict of interest

There are no conflicts of interest.

Author details

Mariana Potcoava[1]*, Christopher Mann[2,3], Jonathan Art[1] and Simon Alford[1]

1 Department of Anatomy and Cell Biology, University of Illinois at Chicago, Chicago, USA

2 Department of Applied Physics and Materials Science, Northern Arizona University, Flagstaff, USA

3 Center for Materials Interfaces in Research and Development, Northern Arizona University, Flagstaff, USA

*Address all correspondence to: mpotcoav@uic.edu

IntechOpen

References

[1] Keller PJ, Ahrens MB. Visualizing whole-brain activity and development at the single-cell level using light-sheet microscopy. Neuron. 2015;**85**(3):462-483

[2] Ji N, Freeman J, Smith SL. Technologies for imaging neural activity in large volumes. Nature Neuroscience. 2016;**19**(9):1154-1164

[3] Chen B-C, Legant WR, Wang K, Shao L, Milkie DE, Davidson MW, et al. Lattice light-sheet microscopy: Imaging molecules to embryos at high spatiotemporal resolution. Science. 2014;**346**(6208):1257998

[4] Liang Gao LS, Chen B-C, Betzig E. 3D live fluorescence imaging of cellular dynamics using Bessel beam plane illumination microscopy. Nature Protocols. 2014;**9**:1083-1101

[5] Potcoava M, Mann C, Art J, Alford S. Spatio-temporal performance in an incoherent holography lattice light-sheet microscope (IHLLS). Optics Express. 2021;**29**(15):23888-23901

[6] Potcoava M, Art J, Alford S, Mann C. Deformation measurements of neuronal excitability using incoherent holography lattice light-sheet microscopy (IHLLS). Photonics. 2021;**8**(9):383

[7] Rosen J, Alford S, Anand V, Art J, Bouchal P, Bouchal Z, et al. Roadmap on recent progress in FINCH technology. Journal of Imaging. 2021;**7**(10)

[8] Kim MK. Principles and techniques of digital holographic microscopy. SPIE Reviews. 2010;**1**(1):18005

[9] Kim MK, Yu LF, Mann CJ. Interference techniques in digital holography. Journal of Optics A: Pure and Applied Optics. 2006;**8**(7):S518-SS23

[10] Cuche E, Bevilacqua F, Depeursinge C. Digital holography for quantitative phase-contrast imaging. Optics Letters. 1999;**24**(5):291-293

[11] Mann C, Yu L, Lo CM, Kim M. High-resolution quantitative phase-contrast microscopy by digital holography. Optics Express. 2005;**13**(22):8693-8698

[12] Popescu G, Deflores LP, Vaughan JC, Badizadegan K, Iwai H, Dasari RR, et al. Fourier phase microscopy for investigation of biological structures and dynamics. Optics Letters. 2004;**29**(21):2503-2505

[13] Marquet P, Rappaz B, Magistretti PJ, Cuche E, Emery Y, Colomb T, et al. Digital holographic microscopy: A noninvasive contrast imaging technique allowing quantitative visualization of living cells with subwavelength axial accuracy. Optics Letters. 2005;**30**(5):468-470

[14] Alexander Khmaladze MK, Lo C-M. Phase imaging of cells by simultaneous dual-wavelength reflection digital holography. Optics Express. 2008;**16**:10900-10911

[15] Barer R. Interference microscopy and mass determination. Nature. 1952;**169**(4296):366-367

[16] Popescu G, Park Y, Lue N, Best-Popescu C, Deflores L, Dasari RR, et al. Optical imaging of cell mass and growth dynamics. American Journal of Physiology - Cell Physiology. 2008;**295**(2):C538-CC44

[17] Müller P, Cojoc G, Guck J. DryMass: Handling and analyzing quantitative phase microscopy images of spherical, cell-sized objects. BMC Bioinformatics. 2020;**21**:226

[18] Muller P, Guck J. Response to Comment on "Cell nuclei have lower refractive index and mass density than cytoplasm" a comment on "How a phase image of a cell with nucleus refractive index smaller than that of the cytoplasm should look like?". Journal of Biophotonics. 2018;**11**(6):e201800033

[19] Schurmann M, Scholze J, Muller P, Guck J, Chan CJ. Cell nuclei have lower refractive index and mass density than cytoplasm. Journal of Biophotonics. 2016;**9**(10):1068-1076

[20] Barer R. Refractometry and interferometry of living cells. Journal of the Optical Society of America. 1957;**47**(6):545-556

[21] Belanger E, Levesque SA, Rioux-Pellerin E, Lavergne P, Marquet P. Measuring absolute cell volume using quantitative-phase digital holographic microscopy and a low-cost, open-source, and 3D-printed flow chamber. Frontiers in Physics (Lausane). 2019;**7**:172

[22] Rappaz B, Marquet P, Cuche E, Emery Y, Depeursinge C, Magistretti PJ. Measurement of the integral refractive index and dynamic cell morphometry of living cells with digital holographic microscopy. Optics Express. 2005;**13**(23):9361-9373

[23] Marquet P, Depeursinge C, Magistretti PJ. Exploring neural cell dynamics with digital holographic microscopy. Annual Review of Biomedical Engineering. 2013;**15**: 407-431

[24] Hodgkin AL, Huxley AF. A quantitative description of membrane current and its application to conduction and excitation in nerve. (Reprinted from Journal of Physiology, Vol 117, Pg 500-544, 1952. Bulletin of Mathematical Biology. 1990;**52**(1-2):25-71

[25] Hill RM, Barer J, Hill LL, Butler CM, Harvey DJ, Horning MG. An investigation of recurrent pine oil poisoning in an infant by the use of gas chromatographic-mass spectrometric methods. The Journal of Pediatrics. 1975; **87**(1):115-118

[26] Ramachandran S, Rodriguez S, Potcoava M, Alford S. Single calcium channel nanodomains drive presynaptic calcium entry at lamprey reticulospinal presynaptic terminals. Journal of Neuroscience. 2022;**42**(12): 2385-2403

[27] Rosen J, Brooker G. Digital spatially incoherent Fresnel holography. Optics Letters. 2007;**32**(8):912-914

[28] Rosen J, Brooker G. Non-scanning motionless fluorescence three-dimensional holographic microscopy. Nature Photonics. 2008;**2**:190

[29] Katz B, Rosen J, Kelner R, Brooker G. Enhanced resolution and throughput of Fresnel incoherent correlation holography (FINCH) using dual diffractive lenses on a spatial light modulator (SLM). Optics Express. 2012; **20**(8):9109-9121

[30] Brooker G, Siegel N, Wang V, Rosen J. Optimal resolution in Fresnel incoherent correlation holographic fluorescence microscopy. Optics Express. 2011;**19**(6):5047-5062

[31] Bouchal P, Bouchal Z. Wide-field common-path incoherent correlation microscopy with a perfect overlapping of interfering beams. Journal of the European Optical Society: Rapid Publications. 2013;**8**:13011

[32] Aguet F, Upadhyayula S, Gaudin R, Chou YY, Cocucci E, He KM, et al. Membrane dynamics of dividing cells

imaged by lattice light-sheet microscopy. Molecular Biology of the Cell. 2016; **27**(22):3418-3435

[33] Ga L, Tang WC, Tsai YC, Chen BC. Lattice light sheet microscopy using tiling lattice light sheets. Optics Express. 2019;**27**(2):1497-1506

[34] Hardie RC, Minke B. The trp gene is essential for a light-activated Ca2+ channel in drosophila photoreceptors. Neuron. 1992;**8**(4):643-651

[35] Reuss H, Mojet MH, Chyb S, Hardie RC. In vivo analysis of the drosophila light-sensitive channels, TRP and TRPL. Neuron. 1997;**19**(6): 1249-1259

[36] Huber A, Sander P, Gobert A, Bahner M, Hermann R, Paulsen R. The transient receptor potential protein (Trp), a putative store-operated Ca2+ channel essential for phosphoinositide-mediated photoreception, forms a signaling complex with NorpA, InaC and InaD. The EMBO Journal. 1996;**15**(24): 7036-7045

[37] Ling T, Boyle KC, Zuckerman V, Flores T, Ramakrishnan C, Deisseroth K, et al. High-speed interferometric imaging reveals dynamics of neuronal deformation during the action potential. Proceedings of the National Academy of Sciences of the United States of America. 2020;**117**(19): 10278-10285

[38] Bouchal P, Kapitan J, Chmelik R, Bouchal Z. Point spread function and two-point resolution in Fresnel incoherent correlation holography. Optics Express. 2011;**19**(16): 15603-15620

[39] Rosen J, Siegel N, Brooker G. Theoretical and experimental demonstration of resolution beyond the Rayleigh limit by FINCH fluorescence microscopic imaging. Optics Express. 2011;**19**(27): 26249-26268

[40] Siegel N, Rosen J, Brooker G. Reconstruction of objects above and below the objective focal plane with dimensional fidelity by FINCH fluorescence microscopy. Optics Express. 2012;**20**(18):19822-19835